Research Article | Vol. 25, No. 23 | 13 Nov 2017 | OPTICS EXPRESS 28295
Optics EXPRESS

Broadband infrared absorbers with stacked double chromium ring resonators

HUIXU DENG,[1] LILIANA STAN,[2] DAVID A. CZAPLEWSKI,[2] JIE GAO,[1,3] AND XIAODONG YANG[1,*]

[1]*Department of Mechanical and Aerospace Engineering, Missouri University of Science and Technology, Rolla, MO 65409, USA*
[2]*Center for Nanoscale Materials, Argonne National Laboratory, Argonne, IL 60439, USA*
[3]*gaojie@mst.edu*
**yangxia@mst.edu*

Abstract: A broadband absorber in the infrared wavelength range from 1 μm up to 5 μm is designed and demonstrated with stacked double chromium ring resonators on a reflective chromium mirror. The near-perfect broadband absorption is realized by combining the multilayer impedance match in the short wavelength range and the double plasmonic resonances in the long wavelength range, which is illustrated with an equivalent circuit model for the impedance analysis. The broadband absorber is proved to be angle-insensitive and polarization-independent due to the geometrical symmetry. The thermal analysis for heat generation and temperature distributions inside the absorber structure is also investigated.

OCIS codes: (300.1030) Absorption; (260.5740) Resonance; (130.3060) Infrared; (160.3918) Metamaterials.

References and links

1. Y. Cui, Y. He, Y. Jin, F. Ding, L. Yang, Y. Ye, S. Zhong, Y. Lin, and S. He, "Plasmonic and metamaterial structures as electromagnetic absorbers," Laser Photonics Rev. **8**(4), 495–520 (2014).
2. C. M. Watts, X. Liu, and W. J. Padilla, "Metamaterial electromagnetic wave absorbers," Adv. Mater. **24**(23), OP98–OP120(2012).
3. N. P. Sergeant, O. Pincon, M. Agrawal, and P. Peumans, "Design of wide-angle solar-selective absorbers using aperiodic metal-dielectric stacks," Opt. Express **17**(25), 22800–22812 (2009).
4. H. Wang and L. Wang, "Perfect selective metamaterial solar absorbers," Opt. Express **21**(Suppl 6), A1078–A1093 (2013).
5. S. Molesky, C. J. Dewalt, and Z. Jacob, "High temperature epsilon-near-zero and epsilon-near-pole metamaterial emitters for thermophotovoltaics," Opt. Express **21**(Suppl 1), A96–A110 (2013).
6. W. Chihhui, N. Burton III, J. Jeremy, M. Andrew, Z. Byron, S. Steve, and S. Gennady, "Metamaterial-based integrated plasmonic absorber/emitter for solar thermo-photovoltaic systems," J. Opt. **14**, 024005 (2012).
7. H. Deng, T. Wang, J. Gao, and X. Yang, "Metamaterial thermal emitters based on nanowire cavities for high-efficiency thermophotovoltaics," J. Opt. **16**, 035102 (2014).
8. X. Liu, T. Tyler, T. Starr, A. F. Starr, N. M. Jokerst, and W. J. Padilla, "Taming the Blackbody with Infrared Metamaterials as Selective Thermal Emitters," Phys. Rev. Lett. **107**(4), 045901 (2011).
9. K. A. Arpin, M. D. Losego, A. N. Cloud, H. Ning, J. Mallek, N. P. Sergeant, L. Zhu, Z. Yu, B. Kalanyan, G. N. Parsons, G. S. Girolami, J. R. Abelson, S. Fan, and P. V. Braun, "Three-dimensional self-assembled photonic crystals with high temperature stability for thermal emission modification," Nat. Commun. **4**, 2630 (2013).
10. N. I. Landy, C. M. Bingham, T. Tyler, N. Jokerst, D. R. Smith, and W. J. Padilla, "Design, theory, and measurement of a polarization-insensitive absorber for terahertz imaging," Phys. Rev. B **79**, 125104 (2009).
11. J. B. Pendry, D. Schurig, and D. R. Smith, "Controlling electromagnetic fields," Science **312**(5781), 1780–1782 (2006).
12. K. Aydin, V. E. Ferry, R. M. Briggs, and H. A. Atwater, "Broadband polarization-independent resonant light absorption using ultrathin plasmonic super absorbers," Nat. Commun. **2**, 517 (2011).
13. W. Wang, Y. Cui, Y. He, Y. Hao, Y. Lin, X. Tian, T. Ji, and S. He, "Efficient multiband absorber based on one-dimensional periodic metal-dielectric photonic crystal with a reflective substrate," Opt. Lett. **39**(2), 331–334 (2014).
14. J. W. Dong, G. Q. Liang, Y. H. Chen, and H. Z. Wang, "Robust absorption broadband in one-dimensional metallic-dielectric quasi-periodic structure," Opt. Express **14**(5), 2014–2020 (2006).
15. B. J. Lee and Z. M. Zhang, "Design and fabrication of planar multilayer structures with coherent thermal emission characteristics," J. Appl. Phys. **100**, 063529 (2006).
16. N. Mattiucci, M. J. Bloemer, N. Aközbek, and G. D'Aguanno, "Impedance matched thin metamaterials make metals absorbing," Sci. Rep. **3**, 3203 (2013).

#304224 https://doi.org/10.1364/OE.25.028295
Journal © 2017 Received 8 Aug 2017; revised 30 Sep 2017; accepted 16 Oct 2017; published 31 Oct 2017

Optics EXPRESS

17. H. Deng, Z. Li, L. Stan, D. Rosenmann, D. Czaplewski, J. Gao, and X. Yang, "Broadband perfect absorber based on one ultrathin layer of refractory metal," Opt. Lett. **40**(11), 2592–2595 (2015).
18. Y. Cui, K. H. Fung, J. Xu, H. Ma, Y. Jin, S. He, and N. X. Fang, "Ultrabroadband light absorption by a sawtooth anisotropic metamaterial slab," Nano Lett. **12**(3), 1443–1447 (2012).
19. D. Fei, J. Yi, C. Hao, L. Mo, F. Ding, Y. Jin, B. Li, H. Cheng, L. Mo, and S. He, "Ultrabroadband strong light absorption based on thin multilayered metamaterials," Laser Photonics Rev. **8**(6), 946–953 (2014).
20. J. Zhou, A. F. Kaplan, L. Chen, and L. J. Guo, "Experiment and theory of the broadband absorption by a tapered hyperbolic metamaterial array," ACS Photonics **1**(7), 618–624 (2014).
21. D. Ji, H. Song, X. Zeng, H. Hu, K. Liu, N. Zhang, and Q. Gan, "Broadband absorption engineering of hyperbolic metafilm patterns," Sci. Rep. **4**, 4498 (2014).
22. Y. Sun, B. Edwards, A. Alù, and N. Engheta, "Experimental realization of optical lumped nanocircuits at infrared wavelengths," Nat. Mater. **11**(3), 208–212 (2012).
23. D. Zhu, M. Bosman, and J. K. W. Yang, "A circuit model for plasmonic resonators," Opt. Express **22**(8), 9809–9819 (2014).
24. M. Staffaroni, J. Conway, S. Vedantam, J. Tang, and E. Yablonovitch, "Circuit analysis in metal-optics," Phot. Nano. Fund. Appl. **10**(1), 166–176 (2012).
25. Q. Zhang, L. Bai, Z. Bai, P. Hu, and C. Liu, "Theoretical analysis and design of a near-infrared broadband absorber based on EC model," Opt. Express **23**(7), 8910–8917 (2015).
26. E. D. Palik, *Handbook of Optical Constants of Solids* (Academic, 1985).
27. D. Barchiesi and T. Grosges, "Fitting the optical constants of gold, silver, chromium, titanium, and aluminum in the visible bandwidth," J. Nanophotonics **8**(1), 083097 (2014).
28. A. D. Rakic, A. B. Djurišić, J. M. Elazar, and M. L. Majewski, "Optical properties of metallic films for vertical-cavity optoelectronic devices," Appl. Opt. **37**(22), 5271–5283 (1998).
29. N. Moshonas, G. K. Pagiatakis, and N. A. Stathopoulos, "Application of the transmission line method for the study of highly nonlinear multilayer optical structures," Opt. Eng. **53**(11), 115106 (2015).
30. H. A. Haus, *Waves and Fields in Optoelectronics* (Prentice-Hall, Inc., 1984).
31. D. Cheng, J. Xie, P. Zhou, H. Zhang, N. Zhang, and L. Deng, "Numerical study of a new negative index material in mid-infrared spectrum," Opt. Express **20**(23), 25744–25751 (2012).
32. J. Zhou, E. N. Economon, T. Koschny, and C. M. Soukoulis, "Unifying approach to left-handed material design," Opt. Lett. **31**(24), 3620–3622 (2006).
33. S. Ghosh and K. V. Srivastava, "An Equivalent Circuit Model of FSS-Based Metamaterial Absorber Using Coupled Line Theory," IEEE Antennas Wirel. Propag. Lett.**14**, 511–514 (2015).
34. Y. Pang, H. Cheng, Y. Zhou, and J. Wang, "Analysis and design of wired-based metamaterial absorbers using equivalent circuit approach," J. Appl. Phys. **113**, 114902 (2013).
35. J. Zhou, L. Zhang, G. Tuttle, T. Koschny, and C. M. Soukoulis, "Negative index materials using simple short wire pairs," Phys. Rev. B **73**, 041101 (2006).
36. S. Bhattacharyya, S. Ghosh, and K. V. Srivastava, "Equivalent circuit model of an ultra-thin polarization-independent triple band metamaterial absorber," AIP Adv. **4**, 097127 (2014).
37. J. G. Hong and M. J. Lancaster, *Microstrip Filters for RF/Microwave Applications* (John Wiley & Sons, Inc., New York, 2001).
38. W. Li, U. Guler, N. Kinsey, G. V. Naik, A. Boltasseva, J. Guan, V. M. Shalaev, and A. V. Kildishev, "Refractory Plasmonics with Titanium Nitride: Broadband Metamaterial Absorber," Adv. Mater. **26**(47), 7959–7965 (2014).
39. P. Nagpal, S. E. Han, A. Stein, and D. J. Norris, "Efficient low-temperature thermophotovoltaic emitters from metallic photonic crystals," Nano Lett. **8**(10), 3238–3243 (2008).
40. A. Narayanaswamy and G. Chen, "Surface modes for near field thermophotovoltaics," Appl. Phys. Lett. **82**, 3544–3546 (2003).
41. E. Rephaeli and S. Fan, "Absorber and emitter for solar thermo-photovoltaic systems to achieve efficiency exceeding the Shockley-Queisser limit," Opt. Express **17**(17), 15145–15159 (2009).

1. Introduction

Broadband infrared absorbers have been widely studied recently [1,2] due to their crucial roles in various applications such as solar energy harvesting [3,4], thermophotovoltaic energy conversion [5–7], thermal emission [8,9], thermal imaging [10], and stealth devices [11]. Diverse methods have been considered to obtain broadband absorption based on different mechanisms including the combination of multiple resonances in metasurfaces [4,8,12], exciting interferences in metal-dielectric stacks [3,13–15], achieving impedance match in multilayers with free space [16,17], and the generation of slow light in tapered multilayer waveguides [18–21].

In this paper, a broadband infrared absorber made of stacked double chromium (Cr) ring resonators on a chromium mirror is designed based on the combination of multilayer impedance match in the short wavelength range and the double plasmonic resonances in the

Optics EXPRESS

long wavelength range. The absorber structure is milled from two pairs of Cr-SiO_2 layers with overall thickness of 360 nm on a reflective substrate. Different from combining multiple resonators in the same horizontal plane, the proposed absorber has double Cr ring resonators stacked in the vertical direction. At the same time, the stacked double ring structure can be effectively regarded as one-dimensional metal-dielectric multilayer lattice for satisfying impedance match conditions in the short wavelength range. An equivalent circuit (EC) model is developed to analyze and optimize the broadband absorber according to the transmission line theory for the multilayer impedance in the short wavelength range and the coupled lumped-element LC resonators [22–25] for the resonance impedance in the long wavelength range. The absorption spectra predicted by the EC model agree with both the simulated and measured absorption spectra and can explain the two absorption mechanisms thoroughly. Further investigations on the oblique incidence under different polarizations, resonant mode fields, heat generation and temperature increase are also performed.

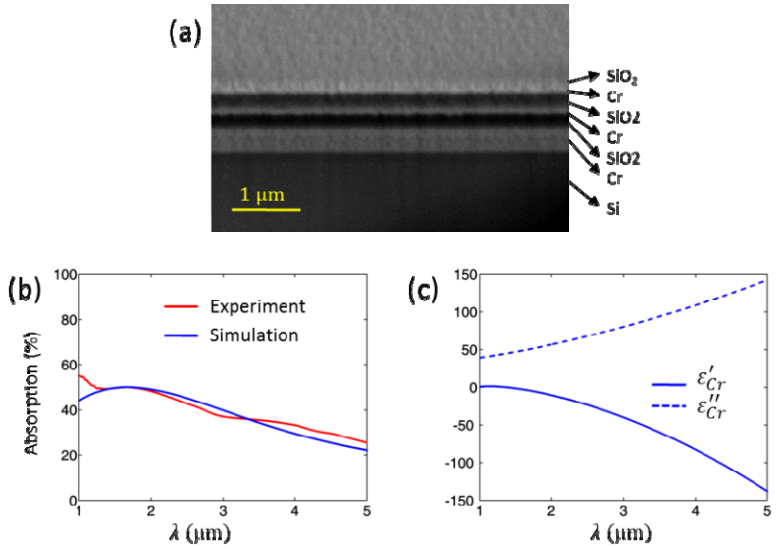

Fig. 1. (a) SEM image of the Cr-SiO_2 multilayer film before milling. (b) Absorption spectra of the multilayer film from both experiment (red curve) and simulation (blue curve). (c) The real (solid curve) and imaginary (dashed curve) parts of Cr permittivity.

2. Absorber design and equivalent circuit model

The designed infrared absorber is based on a multilayer stack consisting of two pairs of Cr-SiO_2 layers with 30 nm thick Cr and 150 nm thick SiO_2 in each pair deposited on top of a 200 nm thick Cr mirror coated on a silicon wafer. There is an additional 30 nm thick SiO_2 protecting layer deposited on top of the multilayer stack to prevent the top Cr layer from oxidation. The multilayer stack is grown by RF sputtering. The Cr is grown in an Ar atmosphere at 5 mTorr pressure at a deposition rate of $0.5\,\text{Å}/\text{sec}$ and the SiO_2 is grown in a 12:1 mixture of Ar:O_2 at a rate of $0.14\,\text{Å}/\text{sec}$. Figure 1(a) shows a scanning electron microscope (SEM) image of the deposited Cr-SiO_2 multilayer before milling where each layer can be clearly seen. The thick Cr mirror will block any transmission through the sample. At first, the absorption spectrum of the multilayer film is measured using Fourier transform infrared spectroscopy (FTIR). As shown in Fig. 1(b), the experimental absorption is below 50% in the range of $1\sim 5\,\mu\text{m}$, which can be matched well with simulation (COMSOL Multiphysics software), by using the Cr permittivity of $\varepsilon_{Cr}=\varepsilon'_{Cr}+i\varepsilon''_{Cr}$ shown in Fig. 1(c)

Optics EXPRESS

calculated according to the Brendel-Bormann model [26–28]. The SiO_2 permittivity is equal to a constant $\varepsilon_{SiO_2} = 2.25$.

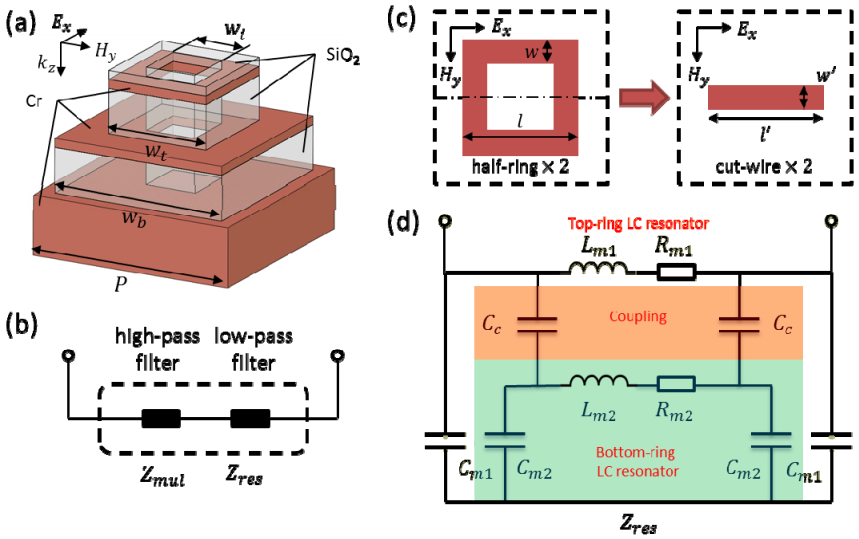

Fig. 2. (a) Schematic of the designed broadband infrared absorber consisting of stacked double Cr ring resonators milled from two pairs of Cr-SiO_2 layers on top of a reflective Cr mirror. (b) Equivalent circuit model of the total impedance for the double-ring absorber consisting of Z_{mul} as a high-pass filter and Z_{res} as a low-pass filter. (c) Transformation of two half-rings of width w and length l into two equal cut-wires of effective width w' and effective length l'. (d) Equivalent circuit for Z_{res} based on the coupled lumped-element LC resonators.

The schematic of the designed absorber with stacked double ring resonators is illustrated in Fig. 2(a). The absorber structure is fabricated using Focused Ion Beam (FIB) milling in two steps. First, the top pair of Cr-SiO_2 layer is milled to form the top ring resonator; and then the bottom pair of Cr-SiO_2 layer is milled to form the bottom ring resonator. During the FIB milling, a SiO_2 layer with very thin thickness is remained on top of the second Cr layer to avoid oxidation. Due to the zero transmission from the absorber, the absorption A is merely determined by the reflection R and is equal to $A = 1 - R$. The Cr layers have the thickness of $t_m = 30\,\text{nm}$ and the two SiO_2 layers have the thickness of $t_d = 150\,\text{nm}$. In one unit cell, the period in x and y directions are both equal to P. For one design, when the period is $P = 700\ \text{nm}$, the top ring width is $w_t = 350\,\text{nm}$ and the bottom ring width is $w_b = 600\,\text{nm}$. The inner hole size of the two rings is the same with $w_i = 175\,\text{nm}$.

An equivalent circuit (EC) model is developed to evaluate the broadband absorption mechanism of the designed double-ring absorber by considering the combination of the multilayer impedance match in the short wavelength range and the double plasmonic resonances in the long wavelength range. The multilayer impedance Z_{mul} can be regarded as a high-pass filter with no reflection at high frequencies and the resonance impedance Z_{res} can be treated as a low-pass filter with no reflection at low frequencies. As shown in Fig. 2(b), the EC model is then built up by adding the two impedances together in series to estimate the total impedance of the absorber, $Z_{tot} = Z_{mul} + Z_{res}$. And the absorption can be calculated as $A = 1 - \left((Z_{tot} - Z_0)/(Z_{tot} + Z_0)\right)^2$, where Z_0 is the impedance of free space.

Optics EXPRESS

Z_{mul} can be evaluated according to the transmission line theory by regarding the double-ring resonators as effective one-dimensional metal-dielectric multilayer lattice in the vertical direction [17,29,30],

$$Z_{mul} = Z(1), \text{ and } Z(j) = \frac{Z_j\left(Z(j+1) - iZ_j \tan\delta_j\right)}{Z_j - iZ(j+1)\tan\delta_j}, j = 1,2,...,6 \qquad (1)$$

where $Z(1)$ represents the wave impedance of the whole multilayer structure seen from the top and can be calculated layer by layer starting from the bottom Cr mirror with the wave impedance of $Z(6)$ up to the top SiO_2 protecting layer with the wave impedance of $Z(1)$, by considering the phase shift δ_j and the characteristic impedance Z_j for each layer j of the multilayer lattice. $\delta_j = f_{pj}\kappa_0 N_j t_j$ in which κ_0 is the wave vector of incident wave, N_j is the complex refractive index and t_j is the layer thickness. Particularly, t_j is modified by a factor f_{pj} to represent the effective layer thickness due to the material milling.

Z_{res} is estimated based on the coupled lumped-element LC resonators. As shown in Fig. 2(c), when the incident light has the field components of E_x and H_y, each ring resonator can be divided into two symmetric half-ring parts [31–33] of width w and length l by the central line and transformed into two cut-wires of effective width w' and effective length l'. Each cut-wire is a LC resonator consisting of three components: inductor L_m, resistor R_m and capacitor C_m. The capacitor C_e due to the electric resonance between two neighboring rings is ignored to simplify the circuit since the magnetic resonance is dominant in this structure [34]. Here, L_m can be expressed as the capacitance between two parallel plates separated by a distance [35], $L_m = a_m\mu_0 l t_d / w$, where μ_0 is the permeability of vacuum and a_m is a numerical factor considering the effective length l' of the cut-wire. $R_m = c_r\rho l/(wt_m)$, where c_r is a numerical factor, and $\rho \equiv 1/\sigma = R' - i\omega L' = -1/(i\omega\varepsilon_0(\varepsilon_m - 1))$ is defined as the combination of intrinsic resistivity R' and inductivity L' [23] of the metal (with relative permittivity of ε_m) since the contribution of the drifting electrons cannot be neglected at infrared frequencies [22,24,33]. C_m is formed between the half-ring and the Cr mirror due to the magnetic resonance and evaluated by the capacitance between two parallel plates separated by the dielectric spacer [32,35], $C_m = b_m\varepsilon_0\varepsilon_d w(0.5l)/t_d$, where ε_0 is the permittivity of vacuum, ε_d is the relative permittivity of the dielectric spacer, and b_m is a numerical factor representing the effective capacitance area.

The equivalent circuit for Z_{res} is shown in Fig. 2(d) consisting of two LC resonators. The first LC resonator includes L_{m1} and R_{m1} representing the top ring and C_{m1} between the top-ring layer and the Cr mirror. The second LC resonator is similar to the first one but it is formed by the middle ring and the Cr mirror including circuit components of L_{m2}, R_{m2} and C_{m2}. Meanwhile, when two ring resonators are placed closely, they are coupled through the capacitor $C_c = b_c\varepsilon_0\varepsilon_d w_1(0.5l_1)/t_d$ between the two rings separated by the dielectric spacer [36,37]. Eventually, the calculated Z_{res} can be expressed as:

$$Z_{res} = \frac{C_c + C_{m2}}{i\omega C_c C_{m2}\left(\frac{(2C_c + C_{m2})(C_{m1}C_{m2} + C_c(C_{m1} + C_{m2}))}{C_c(C_{m2}(C_{m1} + C_{m2}) + C_c(C_{m1} + 3C_{m2}))} + \frac{C_c + C_{m2}}{i\omega C_c C_{m2} R_{m1} - \omega^2 C_c C_{m2} L_{m1}} - \frac{C_c}{C_{m2}(-2 + \omega(C_c + C_{m2})(-iR_{m2} + \omega L_{m2}))}\right)} \qquad (2)$$

Optics EXPRESS

3. Demonstration of broadband infrared absorber

The broadband absorption response of the double-ring absorber can be evaluated by combing the two impedances of Z_{mul} and Z_{res} together. As an example, for the absorber with period of $P = 700$ nm, Fig. 3(a) shows the absorption spectra calculated by the EC model and the simulation result (COMSOL Multiphysics software). In order to fit the simulated resonance peaks of two ring resonators and absorption amplitude, the coefficients used in the EC model for the double-ring absorber with $P = 700$ nm are set as the following: $f_{pj} = 0.8, 0.17, 0.8, 0.33, 0.97$ for each effective layer of $j = 1, 2, 3, 4, 5$ respectively; $a_{m1} = 1.0$, $b_{m1} = 0.8$, $c_{r1} = 0.4$ for the top ring resonator, $a_{m2} = 1.9$, $b_{m2} = 0.75$, $c_{r2} = 0.9$ for the bottom ring resonator, and $b_c = 3.2$ for the coupling of two ring resonators. In the long wavelength range ($2 \sim 5\,\mu$m), the absorption is majorly due to the double ring resonances, and in the short wavelength range ($1 \sim 2\,\mu$m), the absorption is mainly due to the multilayer impedance match condition. To explain the combination of these two absorption mechanisms, Z_{mul}, Z_{res} and Z_{tot} calculated by the EC model are plotted in Fig. 3(b). There are two peaks in the real part of $Z_{res} = Z'_{res} + iZ''_{res}$ located at about $\lambda = 2.1\,\mu$m and $\lambda = 3.7\,\mu$m representing the two Cr ring resonances in the long wavelength range. Correspondingly, two absorption peaks in the range of $\lambda = 2 \sim 5\,\mu$m can be observed in the EC model curve in Fig. 3(a). Additionally, the real part of $Z_{mul} = Z'_{mul} + iZ''_{mul}$ is close to $Z_0 = 1$ at about $\lambda = 1.8\,\mu$m indicating that the multilayer impedance match condition can be achieved in the short wavelength range. The absorption peak of the theoretical absorption in the range of $\lambda = 1 \sim 2\,\mu$m is the intersection of Z_{mul} and Z_{res} resulting from the real part of $Z_{tot} = Z'_{tot} + iZ''_{tot}$ close to $Z_0 = 1$.

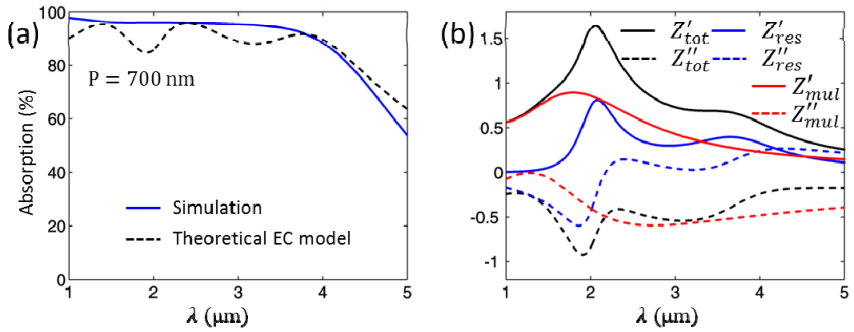

Fig. 3. (a) Comparison of the absorption spectra calculated from the EC model (dashed black curved) and the simulation (blue solid curve) for the double-ring absorber with $P = 700\,\text{nm}$. (b) The corresponding real parts (solid curves) and imaginary parts (dashed curves) of impedances for Z_{mul} (in red), Z_{res} (in blue), and Z_{tot} (in black).

In order to show how the absorption spectrum change with the absorber structure size, three double-ring absorbers with different periods and ring sizes are fabricated. As shown in Figs. 4(a)-4(c), the solid curves are the measured absorption spectra for the double-ring absorbers with periods of $P = 600$ nm (in magenta), $P = 700$ nm (in blue) and $P = 800$ nm (in red), respectively, while the ring dimensions keep the same ratios as $W_{in} = P/4$, $W_t = P/2$, $W_b = l = P - 100(\text{nm})$ (the gap between two neighboring bottom rings is always 100 nm). The dashed curves are the simulated absorption spectra. The insert in each figure is the SEM image of the fabricated double-ring absorber. The absorption spectrum range is

Optics EXPRESS

affected by the period P and the ring length l. When $P = 600\,\text{nm}$ (with ring dimensions of $w_b = 500\,\text{nm}, w_t = 300\,\text{nm}$ and $w_i = 150\,\text{nm}$), the absorption spectrum range with more than 80% absorption is $\lambda = 1 \sim 3.1\,\mu\text{m}$. As P is increased, the absorption spectrum range gets broader but the absorption becomes lower. For $P = 800\,\text{nm}$ (with ring dimensions of $w_b = 700\,\text{nm}, w_t = 400\,\text{nm}$ and $w_i = 200\,\text{nm}$), the absorption spectrum range can reach $\lambda = 1 \sim 4.8\,\mu\text{m}$ for the absorption over 80%. The absorber with $\text{P} = 700\ \text{nm}$ (with ring dimensions of $w_b = 600\,\text{nm}, w_t = 350\,\text{nm}$ and $w_i = 175\,\text{nm}$) is the optimized result by taking account of the trade-off between absorption spectrum range and absorption amount. Its absorption spectrum range can reach $\lambda = 1 \sim 3.75\,\mu\text{m}$ with the absorption over 80%.

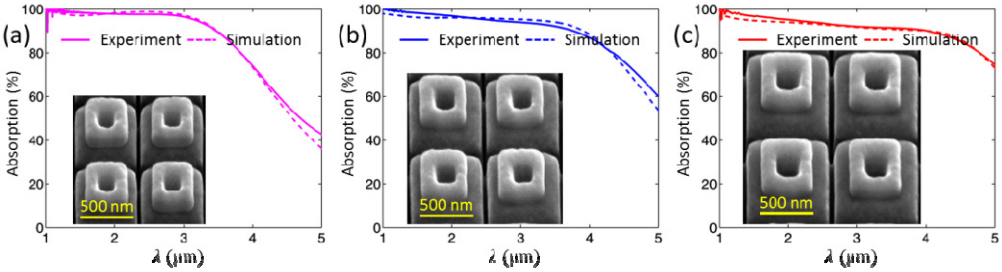

Fig. 4. Experimental (solid curves) and simulated (dashed curves) absorption spectra for the double-ring absorber with (a) $P = 600\,\text{nm}$, (b) $P = 700\,\text{nm}$ and (c) $P = 800\,\text{nm}$, respectively. The insert is the SEM image of the fabricated double-ring absorber structure.

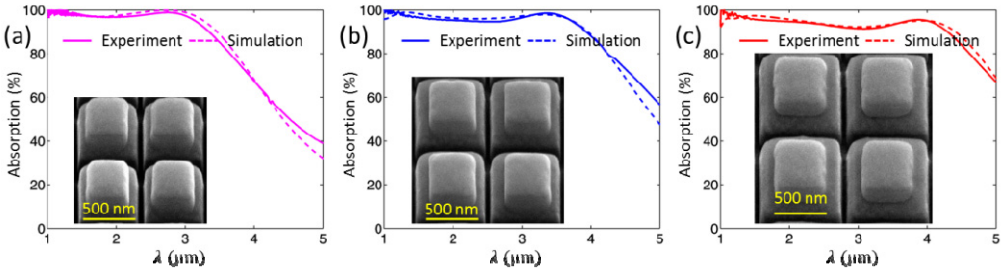

Fig. 5. Experimental (solid curves) and simulated (dashed curves) absorption spectra for the double-square absorber with (a) $P = 600\,\text{nm}$, (b) $P = 700\,\text{nm}$ and (c) $P = 800\,\text{nm}$, respectively. The insert is the SEM image of the fabricated double-square absorber structure.

The double-ring structure will change into double-square structure if the center hole has the zero width, which can make the fabrication process simpler. Similar to the double-ring structure, the double-square structure can also be regarded as two coupled plasmonic resonators. As shown in Fig. 5, the double-square absorbers with the periods of $\text{P} = 600\ \text{nm}$, $\text{P} = 700\ \text{nm}$ and $\text{P} = 800\ \text{nm}$ can also achieve the broadband absorption spectra with absorption above 80% similar to the double-ring absorbers. The absorption spectrum of double-square absorber is not as flat as that of double-ring absorber, but it has a small absorption peak in the long wavelength range.

Oblique incidence is also considered to show if the designed absorber can work in different incident angles and collect more infrared light. Since the double-ring structure is symmetric, the absorption is the same for TE and TM polarizations (configurations as shown in Figs. 6(a) and 6(b)) under normal incidence. However, under oblique incidence, the absorption spectra varies differently for TE and TM polarizations when considering the incident angle from 0° to 85°, as shown in Figs. 6(c) and 6(d) for the absorber with

Optics EXPRESS

P = 700 nm. It is shown that the absorption for TM polarization can be kept around 80% even at high incident angles, while the absorption for TE polarization is not as high as TM polarization but still remains around 70% at high incident angles. This is because the double ring resonances are magnetic resonances and the multilayer impedance match can be sustained better for TM polarization at oblique incidence. In consequence, the designed broadband infrared absorber is angle-insensitive and polarization-independent and thus it is practical for energy harvesting applications.

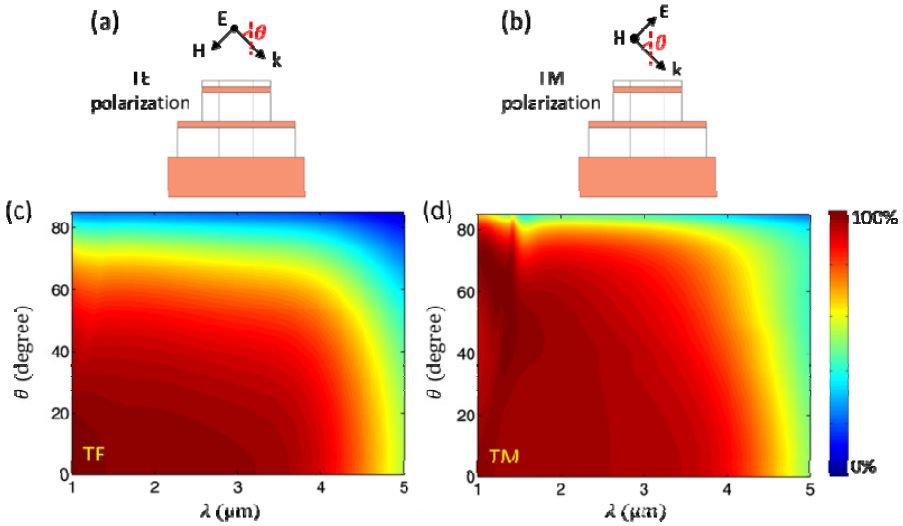

Fig. 6. (a), (b) Configurations of TE polarization and TM polarization. (c), (d) Simulated absorption spectra of the double-ring absorber with $P = 700$ nm under oblique incidence for TE polarization and TM polarization, respectively.

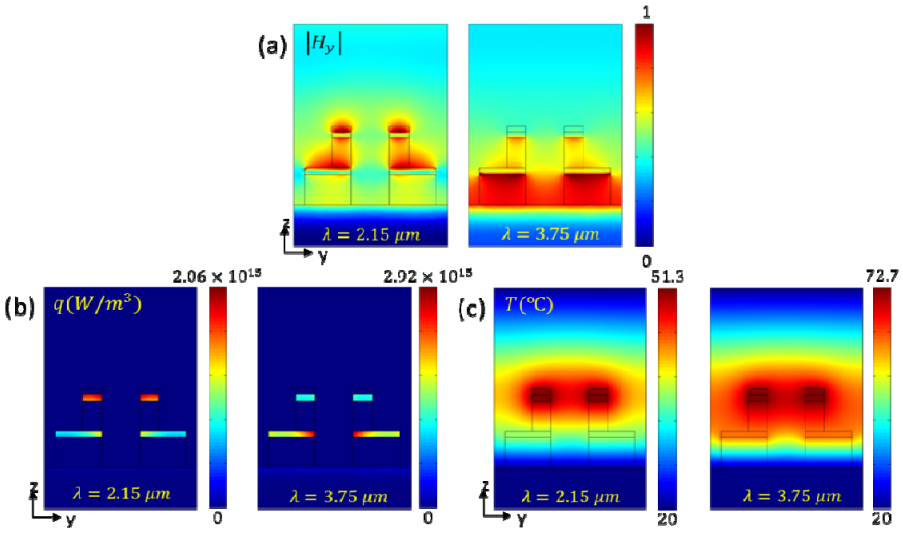

Fig. 7. (a) Normalized magnetic field distributions, (b) heat generation density distributions q and (c) temperature increase distributions T in $y-z$ plane from simulation at $\lambda = 2.15\,\mu\text{m}$ and $\lambda = 3.75\,\mu\text{m}$, respectively, for the double-ring absorber with $P = 700\,\text{nm}$ when the incident power is $20.4\,\mu\text{W}/\mu\text{m}^2$ (corresponding to $10\,\mu\text{W}$ into one unit cell).

Optics EXPRESS

To further explore the two plasmonic resonances of the stacked double Cr ring resonators, optical field distributions are analyzed at the resonant wavelengths using COMSOL Multiphysics software. As shown in Fig. 7(a), the two magnetic resonances can be illustrated with the normalized $|H_y|$ field profiles in $y-z$ plane. At the first magnetic resonance of $\lambda = 2.15\,\mu\text{m}$ dominated by the top ring, the magnetic field is mainly located between the two rings. At the second magnetic resonance of $\lambda = 3.75\,\mu\text{m}$ dominated by the bottom ring, the magnetic field is mostly confined between the bottom ring layer and the Cr mirror.

Particularly in solar thermophotovoltaics (STPV) applications, the device working temperature is usually required to reach at least $800℃$ [38–40] which approaches or even sometimes surpasses the melting points of bulk gold ($1063℃$) and silver ($961℃$) [41]. Chromium with a melting point of $1906℃$ [17] utilized in infrared absorbers can stand high operating temperature. In addition, chromium is significantly cheaper than gold or silver, making chromium a reasonable choice for high-volume production of infrared absorbers. In the broadband absorber, incident light will be eventually converted into heat because of the resistive loss (R_m) of metal. In this way, the Cr ring resonators act as nanoscale heat sources resulting in the local temperature increase and eventually a thermal equilibrium will be reached since the heat is conducted away by air above the absorber structure and the Cr mirror below. To investigate the temperature distribution in the absorber, the heat transfer equation $\nabla\cdot(-k\nabla\theta) = q$ is solved, where k is the thermal conductivity and q is the heat power density generated in the Cr layers, $q(\boldsymbol{r}) = (\omega/2)\,\text{Im}[\varepsilon(\omega)]\varepsilon_0|\boldsymbol{E}(\boldsymbol{r})|^2$. As shown in Fig. 7(b), when the incident single-wavelength plane wave at $\lambda = 2.15\,\mu\text{m}$ matching the top ring resonance is used with the incident power of $20.4\,\mu\text{W}/\mu\text{m}^2$ (corresponding to $10\,\mu\text{W}$ optical power into each unit cell), the maximum heat generation density is about $2.06\times10^{15}\,\text{W/m}^3$ located at the top ring. When the wavelength of incident plane wave is tuned to match the bottom ring resonance at $\lambda = 3.75\,\mu\text{m}$, the maximum heat generation density can reach $2.92\times10^{15}\,\text{W/m}^3$ located at the bottom ring. At thermal equilibrium, the temperature increase distribution is a result of the balance between the heat generation and the boundary conditions where heat is conducted away. In simulation, the top and bottom boundaries are set as the fixed temperature and the side boundaries are insulated since the structure is periodic. The temperature increase distributions are plotted in Fig. 7(c) at the two resonant wavelengths. According to the Fourier's law where heat transfer rate is proportional to the thermal conductivity of material and the temperature gradient as well, the highest temperature $51.3℃$ is located in the top-ring for $\lambda = 2.15\,\mu\text{m}$ since heat is mostly generated in the top ring. However, for $\lambda = 3.75\,\mu\text{m}$, temperature increase in the top ring is still high (reaching to $72.7℃$) although heat is mainly generated in the bottom ring. This is because the bottom ring is close to the Cr mirror with high thermal conductivity, while dielectric layer and air has a much lower thermal conductivity.

4. Conclusion

A broadband infrared absorber consisting of stacked double Cr ring resonators on a Cr mirror has been designed and demonstrated with an average absorption more than 80% in 1 ~5 μm spectrum range. It is made of the refractory metal Cr based on the combination of two absorption mechanisms: the multilayer impedance match in the short wavelength range and the double plasmonic resonances in the long wavelength range. An equivalent circuit model has been constructed to analyze the impedance of the absorber. The designed absorber is proved to be angle-insensitive and polarization-independent under oblique incidence so that more light can be collected under different situations. The demonstrated Cr based absorber

Optics EXPRESS

can work in high temperature environments due to the high melting point of Cr. The demonstrated broadband Cr double-ring absorber in infrared wavelength range will advance the relevant applications such as thermophotovoltaics, solar thermophotovoltaics, thermal detection, and thermal imaging.

Funding

National Science Foundation (NSF) (DMR-1552871, ECCS-1653032); Office of Naval Research (ONR) (N00014-16-1-2408); U.S. Department of Energy, Office of Science, under Contract No. DE-AC02-06CH11357).

Acknowledgment

The authors acknowledge the facility support from the Materials Research Center at Missouri S&T. This work was performed, in part, at the Center for Nanoscale Materials, a U.S. Department of Energy Office of Science User Facility, and supported by the U.S. Department of Energy, Office of Science, under Contract No. DE-AC02-06CH11357.